

## Article

# Using $^{137}\text{Cs}$ and $^{210}\text{Pb}_{\text{ex}}$ to Investigate the Soil Erosion Moduli of the Sandy Area of Typical Grasslands in Northern China

Xuan Guo <sup>1,2</sup>, Yunfeng Hu <sup>1,2,\*</sup> , Yunzhi Zhang <sup>1,2</sup>  and Lin Zhen <sup>2,3</sup>

<sup>1</sup> State Key Laboratory of Resources and Environmental Information System, Institute of Geographic Sciences and Natural Resources Research, CAS, Beijing 100101, China

<sup>2</sup> College of Resources and Environment, University of Chinese Academy of Sciences, Beijing 100049, China

<sup>3</sup> Key Laboratory for Resources Use & Environmental Remediation, Institute of Geographic Science and Natural Resources Research, CAS, Beijing 100101, China

\* Correspondence: huyf@lreis.ac.cn

**Abstract:** Soil erosion results in land degradation and desertification in northern China. The Xilingol League of Inner Mongolia is an important part of the “Two Barriers and Three Belts”, and has been given the main function of “a windbreak and sand-fixing belt of northern China”. Accurate measuring of soil erosion moduli, analyzing the differences in soil erosion moduli across different periods and regions, are the basis for carrying out soil conservation and evaluating the effectiveness of ecological governance. Some radioisotopes are good environmental tracers because they are closely combined with the fine particles of the surface soil and are only affected by the mechanical movement of soil particles. In this paper, Taipusi Banner and Zhengxiangbai Banner, which are in the farming–pastoral ecotone in northern China, were selected as the study area. A regional reference inventory, that is, the activity of  $^{137}\text{Cs}$  and  $^{210}\text{Pb}_{\text{ex}}$  in the sample without any soil erosion, accumulation/deposition, or any kind of manual disturbances, as well as the soil erosion moduli, were determined by  $^{137}\text{Cs}$  and  $^{210}\text{Pb}_{\text{ex}}$  composite tracing technology and multiple lines of evidence. The results are as follows: (1) The regional  $^{137}\text{Cs}$  reference inventory was  $1928 \text{ Bq}\cdot\text{m}^{-2}$ , and the regional  $^{210}\text{Pb}_{\text{ex}}$  reference inventory was  $10,041 \text{ Bq}\cdot\text{m}^{-2}$ . (2) On a 50-year time scale, the soil erosion moduli in the study area ranged from  $140 \text{ t}\cdot\text{km}^{-2}\cdot\text{a}^{-1}$  to  $1030 \text{ t}\cdot\text{km}^{-2}\cdot\text{a}^{-1}$ ; on a 100-year scale, the soil erosion moduli in the study area ranged from  $35 \text{ t}\cdot\text{km}^{-2}\cdot\text{a}^{-1}$  to  $2637 \text{ t}\cdot\text{km}^{-2}\cdot\text{a}^{-1}$ ; the entire study area was in a lightly eroded state. (3) Compared with two periods before and after the 1970s, the southern parts (cultivated land and grassland) experienced an increasing trend in soil erosion moduli due to land reclamation, grassland grazing, and other activities. Due to weakening wind and increasing precipitation, soil erosion moduli in the northern parts (southern margin of the Hunshandake Sandy Land) slowed down. The study also discussed the uncertainty and application potential of isotope-tracing technology in sandy land of typical grasslands in northern China.

**Keywords:** farming–pastoral ecotone; isotope tracer; reference inventory; erosion moduli; dynamic change



**Citation:** Guo, X.; Hu, Y.; Zhang, Y.; Zhen, L. Using  $^{137}\text{Cs}$  and  $^{210}\text{Pb}_{\text{ex}}$  to Investigate the Soil Erosion Moduli of the Sandy Area of Typical Grasslands in Northern China. *Sustainability* **2022**, *14*, 12137. <https://doi.org/10.3390/su141912137>

Academic Editor: Teodor Rusu

Received: 6 September 2022

Accepted: 20 September 2022

Published: 25 September 2022

**Publisher’s Note:** MDPI stays neutral with regard to jurisdictional claims in published maps and institutional affiliations.



**Copyright:** © 2022 by the authors. Licensee MDPI, Basel, Switzerland. This article is an open access article distributed under the terms and conditions of the Creative Commons Attribution (CC BY) license (<https://creativecommons.org/licenses/by/4.0/>).

## 1. Introduction

The Xilingol League of Inner Mongolia, located in the middle of the farming–pastoral ecotone in northern China, is an important part of the “Two Barriers and Three Belts”, and has been given the main function of “a windbreak and sand-fixing belt of northern China”. This functional positioning is not only related to the sustainable development of local grassland animal husbandry and farmland planting but is also of great significance for ensuring ecological safety and air quality of northern China and even the entire East Asia region. Due to global climate change, intensifying human land reclamation and grazing activities, the region has experienced increasingly serious ecological and environmental problems, such as grassland degradation, soil desertification, and frequent sandstorms,

since the 1980s. Soil erosion with wind erosion are important causes of land degradation, desertification, and dusty weather in this area [1,2]. Since 2000, the Chinese government has carried out ecological management and restoration projects, namely, the Returning Grazing Land to Grassland project, the North Shelter Forest, and the Natural Forest Protection project, achieving major results. The quality of the local and downwind ecological environment has been significantly improved [3,4]. Therefore, accurately assessing the soil erosion situation in the farming–pastoral ecotone in northern China, and quantitatively measuring the dynamic changes in soil erosion moduli, are of great significance to the restoration of degraded land and the construction of ecological civilization.

At present, the global research on soil erosion has changed from qualitative to quantitative. Relevant research methods are becoming more and more abundant; for example, remote sensing combined with USLE and RUSLE model methods, to achieve soil erosion moduli measurements using high-tech, although these are still subject to the limitations of remote sensing image resolution and scale, and thus field sampling data are required to verify the model results [5–7]. The rare earth element tracing method (REE) is used to measure the concentration of REE and the amount of erosion or deposition of the slope section after a certain erosion time by releasing rare earth elements, which is more used for indoor simulation and small-scale field research [7]. Although the runoff plot method can calculate the law of soil and water loss on a slope, the cost of time, funds, and energy required are relatively high [8]. The geomorphological research method mainly judges the degree of soil erosion qualitatively by observing the geomorphological phenomena related to soil erosion in the field [7]. Although the artificial rainfall simulation method can save manpower, material resources, and time costs, it is difficult to apply the artificial rainfall simulation device in large-scale field experiments [5,9]. The isotope-tracing method is mainly used to collect soil samples at the site to obtain information on the erosion and deposition status of soil particles in the soil, and then estimate the soil erosion moduli. The choice of research methods varies according to the research scale (over a large spatial scale or small-scale research), the erosion properties (wind erosion, water erosion or farming erosion, etc.), and applicability.

The application of the isotope-tracing method to soil erosion research is relatively mature in theory and technology. Menzel [10] pointed out that some radioisotopes (such as  $^{137}\text{Cs}$ ,  $^{210}\text{Pb}_{\text{ex}}$ ,  $^7\text{Be}$ , etc.) are closely combined with surface fine particles after settling from the atmosphere, and their content in the soil would change accordingly with the transport process of soil materials; therefore, these radioisotopes can be used as ideal tracers for soil erosion or accumulation processes. For  $^{137}\text{Cs}$  isotope-tracing techniques, scientists have conducted more in-depth research and established many quantitative soil erosion models (the empirical model, the proportion model, mass balance model, profile distribution model, diffusion and migration model, etc.), which have been applied in studies related to hydraulic erosion, tillage erosion, and wind erosion worldwide [11–16]. In China, researchers have conducted many soil erosion studies based on  $^{137}\text{Cs}$  tracer techniques in the Loess Plateau [17], the Yangtze River Basin [18,19], the Northeast Plain [20,21], the Tibet Plateau [22], and the southern hilly areas [23]. Most of these studies have concentrated on soil erosion in agricultural cultivation regions caused by hydraulic erosion, whereas in the farming–pastoral ecotone of northern China, which is dominated by wind erosion, researchers have conducted relatively few studies on soil erosion changes caused by natural processes as well as ecological restoration processes [24–26].

On the other hand, since  $^{137}\text{Cs}$  is derived from atmospheric nuclear blasts, its characteristics, including a single source, a lack of supplies, and a short half-life (30.17 a), make  $^{137}\text{Cs}$  increasingly difficult to detect in soil samples. Furthermore, various spatial distribution of tracer isotopes in sandy soils lead to greater uncertainty in the measurement results [25]. Therefore, researchers have been trying to develop alternative isotope technology to  $^{137}\text{Cs}$ .  $^{210}\text{Pb}_{\text{ex}}$  soil tracing technology or combined  $^{137}\text{Cs}$ – $^{210}\text{Pb}_{\text{ex}}$  tracing technology is an important technology that reflects this development trend. There have been some successful cases of soil tracing studies using  $^{210}\text{Pb}_{\text{ex}}$  worldwide [27–33]. For

example, Walling and He [33] applied  $^{210}\text{Pb}_{\text{ex}}$  to measure the erosion moduli of cultivated land in the UK, confirming the potential of using  $^{210}\text{Pb}_{\text{ex}}$  to estimate hydraulic erosion on cultivated land. Benmansour [27] applied  $^{137}\text{Cs}$  and  $^{210}\text{Pb}_{\text{ex}}$  in a Mediterranean agricultural area in Morocco, demonstrating that soil erosion processes have not changed significantly over the last 100 years. In general, the number of  $^{210}\text{Pb}_{\text{ex}}$  soil erosion study cases are much less than that based on  $^{137}\text{Cs}$ , and its application is not as extensive as the latter, indicating that there are still many technical details worth exploring, such as the  $^{210}\text{Pb}_{\text{ex}}$  reference inventory calculation and the soil erosion measurement models improvement.

Researchers have applied a single-isotope ( $^{137}\text{Cs}$ ) tracing technique combined with a multi-isotope ( $^{137}\text{Cs}$ – $^{210}\text{Pb}_{\text{ex}}$ ) tracing technique to quantify soil erosion in the farming–pastoral ecotone of northern China, particularly, in a typical temperate grassland with a wind-sand area, Inner Mongolia, China. Hu et al. [34] were the first to establish high-precision  $^{137}\text{Cs}$  vertical distribution profiles in grassland and cultivated land in the farming–pastoral ecotone of northern China (Taipusi Banner, Inner Mongolia). Furthermore, Hu measured the soil erosion moduli and pointed out that the application of the  $^{137}\text{Cs}$  soil tracing technique for quantifying soil erosion has important advantages due to the vast land area and invading wind erosion on the Mongolian plateau. Based on the  $^{137}\text{Cs}$  reference inventory estimation model developed by Walling and He [35], Liu et al. [26] established the  $^{137}\text{Cs}$  reference inventory for different areas in the southern and northern parts of the Tariat–Xilingol transect on the Mongolian plateau, and further noted that the wind erosion moduli at two typical grassland sample sites in the southern part of the transect (Xilinhot and Zhengxiangbai, Inner Mongolia) were nearly three times that of the typical grassland sample sites in the northern part of the transect (Bayannur, Mongolia), which may be caused by the differences in population density and livestock carrying capacity. However, directly using the theoretical model to estimate  $^{137}\text{Cs}$  reference inventory without any modification may lead to uncertainty in the results. Qi et al. [36] compared the theoretical model-estimated reference inventory with the measured reference inventory at 66 sample sites in China and found that the theoretical model underestimated the actual reference inventory. Hu et al. [24] further showed that the actual reference inventory was 120–150% of the theoretical model-estimated values in the central-eastern region of Inner Mongolia. This result provides a basis for identifying regional  $^{137}\text{Cs}$  reference points and discerning a reasonable  $^{137}\text{Cs}$  reference inventory interval.

The deposition process of  $^{137}\text{Cs}$  particles mainly occurred in the 1950s and 1970s when the world's major nuclear powers conducted atmospheric nuclear tests, while the deposition of  $^{210}\text{Pb}_{\text{ex}}$  series particles have been occurring for a long time in nature, potentially being continuously replenished; thus, the erosion rates measured by  $^{137}\text{Cs}$  and  $^{210}\text{Pb}_{\text{ex}}$  as soil tracers reflect the soil erosion process on a short time scale (since the 1970s; that is, a 50-year scale) and long-term scale (a scale of more than 100 years). Therefore, the composite tracer of the above two isotopes can clearly analyze the dynamic characteristics of soil erosion. Hu and Zhang [25] also developed a combined  $^{137}\text{Cs}$ – $^{210}\text{Pb}_{\text{ex}}$  tracing method and estimated soil erosion moduli in the southern margin of Hunsandake, Inner Mongolia. The results showed that wind and sand activity in the southern margin of the Hunsandake sandy land has significantly weakened over the past 50 years. In addition, based on the information of the  $^{137}\text{Cs}$  and  $^{210}\text{Pb}_{\text{ex}}$  reference inventory provided by the established literature, Wang et al. [5] carried out an analysis of the effectiveness of soil conservation by regional ecological management and construction. The results concluded that soil erosion moduli in cultivated and fallow lands were significantly reduced after the implementation of ecological projects, even converting some lands from being in a soil erosion state to a soil-accumulation state.

From a comprehensive analysis of the global and northern China farming–pastoral ecotone, it can be concluded that the application of the  $^{137}\text{Cs}$ – $^{210}\text{Pb}_{\text{ex}}$  combined tracing method for quantitative soil erosion assessment has become the frontier of soil isotope-tracing research. Using the characteristics of the different decay cycles of the two tracer isotopes, to measure and compare changes in soil erosion moduli on different periods, is

crucial to analyze the evolution of the characteristics of soil erosion processes, especially to evaluate the effectiveness of ecological restoration and governance projects. In this paper, two soil tracer isotopes,  $^{137}\text{Cs}$  and  $^{210}\text{Pb}_{\text{ex}}$ , were applied to quantify soil erosion moduli and conduct comparative analysis in the farming–pastoral ecotone of northern China. Our specific objectives were to answer the following questions: (1) How do one select background plots and determine a reference inventory based on multiple characteristics? (2) How does soil erosion or accumulation vary on different time scales? (3) What are the main factors contributing to the uncertainty of the study results?

## 2. Study Area and Method

### 2.1. Study Area

Xilingol League is located at the southeastern margin of the Mongolian Plateau and the east-central part of the Inner Mongolia Autonomous Region, China. The sampling plots were selected from Taipusi Banner and Zhengxiangbai Banner (Figure 1), which are adjacent to Zhenglan Banner to the east, bordering Xianghuang Banner and Huade County to the west, Guyuan County to the south, and Sunitezuo Banner and Abaga Banner to the north. The study region lies between  $114.2^\circ\text{E}$ – $115.9^\circ\text{E}$  and  $41.5^\circ\text{N}$ – $43.1^\circ\text{N}$ .

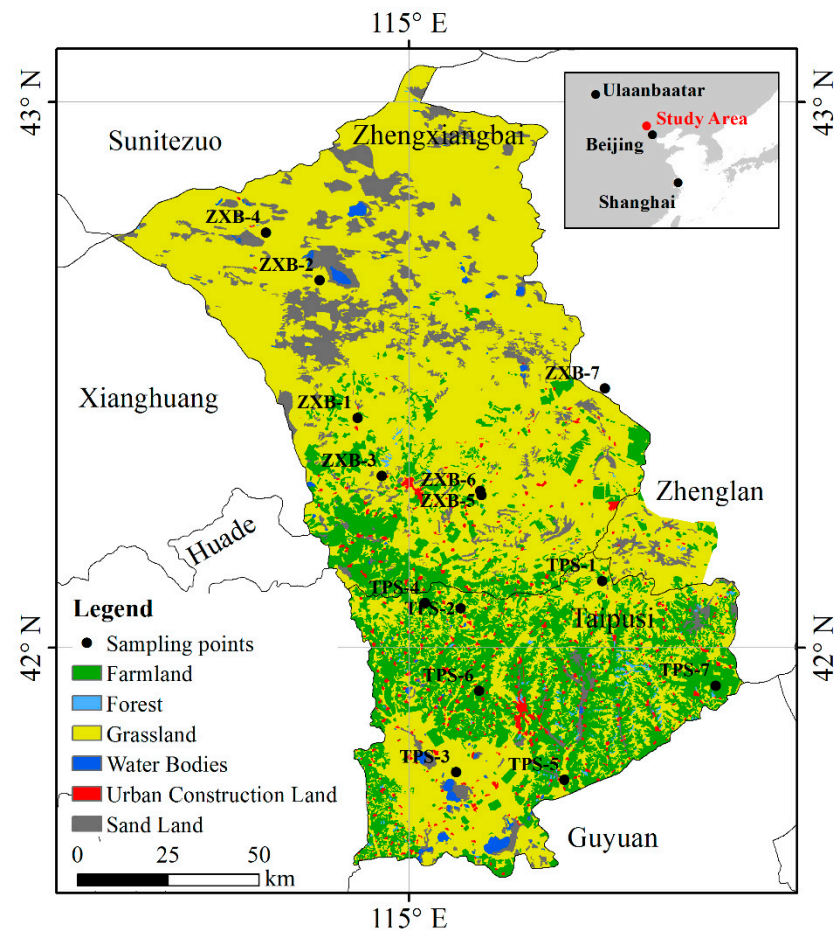


**Figure 1.** The location, land cover characteristics, and sample-point distribution in the study area.

The study area has a temperate continental monsoon climate. Springs are windy and dry, summers are warm and short, autumns are cool, and winters are cold and long. The annual average precipitation is about 343 mm. From south to north, the dryness of the climate gradually increases, and the soil type gradually changes from grassland chestnut-calcium soil to grassland wind-sand soil. The southern part is mainly covered by high plain grassland and dry cultivated land, while the northern part mainly presents fixed,

semi-fixed, semi-shifting sandy and dune landform types. The study area also has a small amount of forest, water bodies, and other surface cover types scattered throughout.

## 2.2. Sampling and Testing

We collected 14 soil samples from 21 to 23 October 2018, with 7 sample plots each in Taipusi Banner and Zhengxiangbai Banner (Figure 1). There were 5 sample plots and 9 sample plots in cultivated land and grassland, respectively. On the other hand, 2 sample plots were in semi-shifting sandy land and 3 sample plots were in fixed sandy land.

The sample plots are generally set in flat and open areas, and the specific locations are determined according to different topographical conditions (semi-shifting sandy land, shifting sandy land, semi-fixed sandy land, and fixed sandy land, etc.) and surface cover (high coverage grassland, medium coverage grassland, low coverage grassland, cultivated land, and fallow land, etc.).

After clearing the ground vegetation and litter, 4 groups of soil samples were collected at each plot according to the triangular distribution method: 3 full-profile samples were excavated at vertexes of the triangle by a soil driller with an internal diameter of 35 mm and a maximum sampling depth of 30 cm; a suite of layer samples were collected at the center via the stratified stripping method. For the layer samples, a layer thickness of 3 cm was used for the top 0–15 cm column, a layer thickness of 5 cm was used for the 15–20 cm column, and a thickness of 10 cm was used for the lowermost 20–30 cm column. The depth was set at 30 cm for the whole sample collection, and the mean values of the 3 sets of full-profile sample data at each plot were calculated statistically in the subsequent data processing.

A low-background photon ( $\gamma$ -ray) multi-channel (214) energy spectrometer from EURISYS, France, was used for soil isotope activity detection, equipped with high purity germanium (HPGe) well probe, with a germanium crystal activity volume of 114 cm<sup>3</sup>, a diameter of 5.5 cm, and height of 6.0 cm. The effective detection depth was 4.1 cm, the inner diameter was 1.5 cm, and the detection  $\gamma$ -ray energy covered 15–2084 keV. A total of 8–10 g of the dried sample was packed into a plastic test tube with an inner diameter of 1.5 cm before testing. After sealing for 20 days, we measured it using the HPGe probe for more than 24 h. The minimum detection limit activity was 0.5 dpm, at the 99% confidence level. According to the national standard of the  $\gamma$ -ray spectrum analysis for soil radionuclides (GB 08304), the activities of <sup>210</sup>Pb<sub>ex</sub> and <sup>137</sup>Cs were obtained by counting the  $\gamma$ -rays with energies of 46.5 keV and 662 keV (<sup>137</sup>Ba–m) in the energy spectrum, respectively.

The activity information obtained from the instrument measurements is the activity value per unit mass (Bq·kg<sup>-1</sup>). Combined with soil bulk density and sampling depth, this can be converted to an area-based isotopic activity value (Bq·m<sup>-2</sup>). For the layer samples, the area-based cumulative isotopic activity of <sup>137</sup>Cs and <sup>210</sup>Pb<sub>ex</sub> can be calculated from the following formula:

$$CPI(PPI) = \sum_{i=1}^n 1000 \times M_i \times N_i \times D_i \quad (1)$$

where *CPI* (<sup>137</sup>Cs point inventory) or *PPI* (<sup>210</sup>Pb<sub>ex</sub> point inventory) is the total activity of <sup>137</sup>Cs and <sup>210</sup>Pb<sub>ex</sub> at the sample point (Bq·m<sup>-2</sup>); *i* is the layer number of the sampling layer; *n* is the number of sampling layers; *M<sub>i</sub>* is the isotope activity of <sup>137</sup>Cs and <sup>210</sup>Pb<sub>ex</sub> at layer *i* (Bq·kg<sup>-1</sup>); *N<sub>i</sub>* is the bulk density of layer *i* (t·m<sup>-3</sup>); and *D<sub>i</sub>* is the sampling depth of layer *i* (m).

For the full-profile samples, the total activity of <sup>137</sup>Cs and <sup>210</sup>Pb<sub>ex</sub> per unit area can be calculated by the following equation:

$$CPI(PPI) = \frac{M \times W}{S} \quad (2)$$

where *M* is the isotope activity of <sup>137</sup>Cs and <sup>210</sup>Pb<sub>ex</sub> in the whole sample (Bq·kg<sup>-1</sup>); *W* is the total weight of each soil sample after sieving (kg); and *S* is the cross-sectional area of the soil driller (m<sup>2</sup>).

### 2.3. Reference Inventory Determining

The reference inventory (CRI:  $^{137}\text{Cs}$  Reference Inventory; PRI:  $^{210}\text{Pb}_{\text{ex}}$  Reference Inventory), also known as background values, refers to the activities of  $^{137}\text{Cs}$  and  $^{210}\text{Pb}_{\text{ex}}$  in the sample without any soil erosion, accumulation/deposition, or any kind of manual disturbances. It is crucial to measure reliable regional CRI or PRI to estimate the soil erosion modulus, to analyze the soil erosion dynamics.

In an earlier-proposed method, a small number of plots are selected through field investigations and on-site observations, and then the mean CPI (or PPI) of them is regarded as the regional CRI (or PRI). Considering the relationship model between  $^{90}\text{Sr}$  atmospheric deposition and precipitation, Walling analyzed the relationship between CRI and precipitation in different spots around the world and proposed a model to estimate CRI globally. However, Qi et al. [36] systematically compared the estimated values of this model with the measured values in China and concluded that the model normally underestimates the actual CRI. Hu et al. [24] further pointed out that the measured CRI in Inner Mongolia was about 120–150% of the model estimates. The above studies provide an important basis for discerning the accuracy and reasonableness of the measured CRI; they also provide support for modifying the model estimates and determining the regional CRI in the absence of accurate and reliable background points.

In this study, we consciously selected high coverage grasslands as alternative background points based on actual land-cover/land-use information. Then we compared the difference between the CPI values from the alternative background points and the model-estimated CRI value to determine whether the CPI values fall within the potential CRI interval (120–150% of the model values). Finally, we also investigated the  $^{137}\text{Cs}$  distribution characteristics in the soil profile. Combining the information from the above three aspects, the background sample plots and regional  $^{137}\text{Cs}$  reference inventory can be determined. Furthermore, we also took the  $^{137}\text{Cs}$  background sample plots as the  $^{210}\text{Pb}_{\text{ex}}$  background sample plots and determined the corresponding  $^{210}\text{Pb}_{\text{ex}}$  reference inventory.

### 2.4. Erosion/Accumulation Moduli Measurement

Soil erosion or accumulation moduli, also known as the soil erosion or accumulation rate, is mainly quantified by soil bulk density and annual average soil erosion thickness. Due to the difference in the self-decay rate between  $^{137}\text{Cs}$  and  $^{210}\text{Pb}_{\text{ex}}$  radioisotopes, based on previous research results, this paper uses a profile distribution model (Formulas 3 and 4) and mass balance model (Formula 8) to calculate the soil erosion or accumulation thickness at different time scales at each sampling point, and further calculate the soil erosion or accumulation moduli (soil erosion or accumulation rate).

The calculation of the  $^{137}\text{Cs}$  soil erosion modulus in grassland was performed using a profile distribution model [16,34,37]. The model is as follows:

$$X = X_0 \times e^{-\lambda \cdot h \cdot (T-1963)} \quad (3)$$

$$X_0 = \text{CRI} \times k \quad (4)$$

where  $X_0$  is the modified  $^{137}\text{Cs}$  reference inventory ( $\text{Bq} \cdot \text{m}^{-2}$ ), which is the result of performing the wind and snow distribution influence ( $k = 0.95$ ) on the CRI;  $X$  is the  $^{137}\text{Cs}$  activity at the current sampling plot ( $\text{Bq} \cdot \text{m}^{-2}$ );  $T$  is the sampling year, which is 2018 in this study;  $\lambda$  is the morphological parameter of the  $^{137}\text{Cs}$  distribution curve, with depth in the background plot profile (Qi et al., 2008), and which can be obtained from the layer-by-layer  $^{137}\text{Cs}$  activity values and fitted by the least-square method; and  $h$  is the annual average soil erosion thickness ( $\text{cm} \cdot \text{a}^{-1}$ ) at the sampling plots since 1963 (the peak year of  $^{137}\text{Cs}$  deposition).

After obtaining the average annual soil erosion thickness, the soil erosion modulus can be calculated by the following equation:

$$E = 10000 \times N \times h \quad (5)$$

where  $E$  is the soil erosion modulus ( $\text{t}\cdot\text{km}^{-2}\cdot\text{a}^{-1}$ ); and  $N$  is the soil bulk density ( $\text{t}\cdot\text{m}^{-3}$ ).

Currently, several models apply  $^{210}\text{Pb}_{\text{ex}}$  to measure soil erosion moduli [38–40]. Considering the continuous sedimentation process and the decay and loss processes of  $^{210}\text{Pb}_{\text{ex}}$ , Zhang et al. [41] derived a mass balance model by measuring the steady distribution state of  $^{210}\text{Pb}_{\text{ex}}$  in uncultivated soils. Sun et al. [42] simplified the model and established a new formula to depict the relationship between the soil erosion moduli and  $^{210}\text{Pb}_{\text{ex}}$  content in uncultivated soil. The model form is as follows:

$$I = \left( \lambda + 1 - e^{-\frac{h}{H}} \right) \times A \quad (6)$$

$$I = \lambda \times A_{\text{ref}} \quad (7)$$

where  $A_{\text{ref}}$  is the  $^{210}\text{Pb}_{\text{ex}}$  reference inventory ( $\text{Bq}\cdot\text{m}^{-2}$ );  $A$  is the total area activity of  $^{210}\text{Pb}_{\text{ex}}$  in the current sampling plot ( $\text{Bq}\cdot\text{m}^{-2}$ );  $I$  is the  $^{210}\text{Pb}_{\text{ex}}$  sedimentation flux ( $\text{Bq}\cdot\text{m}^{-2}\cdot\text{a}^{-1}$ );  $\lambda$  is the  $^{210}\text{Pb}_{\text{ex}}$  decay coefficient ( $0.031\cdot\text{a}^{-1}$ );  $H$  is the relaxation depth ( $\text{kg}\cdot\text{m}^{-2}$ ); and  $h$  is the multi-year average erosion mass thickness ( $\text{kg}\cdot\text{m}^{-2}\cdot\text{a}^{-1}$ ).

From the above two equations, the multi-year average erosion mass thickness ( $\text{kg}\cdot\text{m}^{-2}\cdot\text{a}^{-1}$ ) of  $^{210}\text{Pb}_{\text{ex}}$  is derived as follows:

$$h = -H \times \ln \left( \lambda + 1 - \frac{\lambda \cdot A_{\text{ref}}}{A} \right) \quad (8)$$

Therefore, applying a simple inversion formula, the soil erosion modulus can be roughly calculated for two different periods—1920s–1970s and 1970s–present—by following Equation (9):

$$E_{100} = (E_a + E_b) / 2 \quad (9)$$

where  $E_{100}$  is the soil erosion modulus at the 100-year scale, which is measured by the  $^{210}\text{Pb}_{\text{ex}}$  tracer method;  $E_a$  is the soil erosion modulus at the 50-year scale (1970s–present), which is measured by the  $^{137}\text{Cs}$  tracer method; and  $E_b$  is the soil erosion modulus for the 1920s–1970s period.

### 3. Results

#### 3.1. $^{137}\text{Cs}$ Distribution Characteristics and Reference Inventory

Based on the CRI estimation software, the theoretical value of CRI in the study area is  $1404 \text{ Bq}\cdot\text{m}^{-2}$ . Further considering the amplification coefficient of the measured CRI in the Inner Mongolia Plateau relative to the model simulation value, we determined that the reasonable range of CRI values in the study area is  $1684\sim 2167 \text{ Bq}\cdot\text{m}^{-2}$  (Table 1).

Among all 14 sample plots, only the CPI value of sample plot ZXB-3 was within the above value range. Further investigation of the  $^{137}\text{Cs}$  distribution characteristics at this plot showed that the  $^{137}\text{Cs}$  activity of sample plot ZXB-3 was the highest in the surface soil (3–6 cm) and decreased regularly with increasing depth (Figure 2). These values exhibited the typical distribution type, characterized by “a single peak + a negative exponential curve”, indicating ZXB-3 is a typical  $^{137}\text{Cs}$  background sample plot. Therefore, by combining four types of information, including soil type (chestnut calcium soil), land cover (grassland),  $^{137}\text{Cs}$  activity value, and  $^{137}\text{Cs}$  distribution characteristics, sample plot ZXB-3 can be identified as a background sample plot, and the CPI ( $1927.9 \text{ Bq}\cdot\text{m}^{-2}$ ) of sample plot ZXB-3 can be seen as the CRI.

In addition to the ZXB-3 sample plot, we also investigated the CPI and  $^{137}\text{Cs}$  distribution characteristics of the remaining sample plots.

The analysis showed that, for sample plots ZXB-1, ZXB-2, ZXB-4, ZXB-5, ZXB-6, ZXB-7, TPS-1, and TPS-3, the measured CPI values were lower than the inferred CRI interval from the theoretical model. Although the distribution of the  $^{137}\text{Cs}$  profiles showed a “negative exponential” or “single peak + a negative exponential curve” pattern, the maximum occurrence depth of  $^{137}\text{Cs}$  was very shallow (less than 20 cm), which was much

shallower than the normal occurrence depth of 25–30 cm. Therefore, by combining land cover characteristics, total CPI, and  $^{137}\text{Cs}$  distribution characteristics, the above eight sample plots can be regarded as eroded sandy land/grassland plots.

**Table 1.** The model-estimated value, potential CRI range, and measured CPIs.

Plot	Longitude (°E)	Latitude (°N)	Elevation (m)	Soil	Topography and Land Use	Annual Rainfall (mm)	Model Estimated CRI ( $\text{Bq}\cdot\text{m}^{-2}$ )	Potential CRI Range ( $\text{Bq}\cdot\text{m}^{-2}$ )	Measured CPI ( $\text{Bq}\cdot\text{m}^{-2}$ )	Is the Measured CPI Fall within the Potential CRI
ZXB-1	114.87	42.42	1292.6	Chestnut soil	Grassland				863.1	NO
ZXB-2	114.78	42.68	1128	Aeolian sandy soil	Semi-shifting sandy land Grassland				238.3	NO
ZXB-3	114.93	42.32	1357.4	grey cinnamon soil	Grassland	343	1404	1684–2167	1927.9	YES (137%)
ZXB-4	114.65	42.76	1101.4	Aeolian sandy soil	Semi-shifting sandy land Grassland				502.7	NO
ZXB-5	115.18	42.29	1352.7	Chestnut soil	Fixed sandy land Grassland				871.0	NO
ZXB-6	115.18	42.28	1353.6	Chestnut soil	Fixed sandy land Grassland				1353.4	NO
ZXB-7	115.49	42.48	1242.8	Chestnut soil	Semi-shifting sandy land Grassland				378.9	NO
TPS-1	115.48	42.12	1352.7	Chestnut soil	Grassland				1158.4	NO
TPS-2	115.13	42.07	1456.7	Chestnut soil	Cultivated land				991.9	NO
TPS-3	115.12	41.77	1384.7	Chestnut soil	Grassland				568.5	NO
TPS-4	115.04	42.08	1383	Chestnut soil	Cultivated land				304.5	NO
TPS-5	115.38	41.76	1402.9	Meadow soil	Fallow land				735.6	NO
TPS-6	115.17	41.92	1458.5	Chestnut soil	Fallow land				417.1	NO
TPS-7	115.76	41.93	1400.8	Chestnut soil	Fallow land				629.7	NO

For sample plots TPS-2 and TPS-4, the measured CPI values ( $991.9 \text{ Bq}\cdot\text{m}^{-2}$  and  $304.5 \text{ Bq}\cdot\text{m}^{-2}$ ) were significantly smaller than the inferred CRI value interval. In deeper soils, below 21 cm or 15 cm, the  $^{137}\text{Cs}$  activity was extremely small, while the  $^{137}\text{Cs}$  activity of each layer showed a uniform distribution in the upper soils. Therefore, according to the land cover/use characteristics, total CPI, and  $^{137}\text{Cs}$  profile distribution characteristics, it can be determined that sample plots TPS-2 and TPS-4 were regarded as a plot that had inherited the characteristics of a former cropland.

The measured CPI values in the TPS-5, TPS-6, and TPS-7 sample plots ( $735.6 \text{ Bq}\cdot\text{m}^{-2}$ ,  $417.1 \text{ Bq}\cdot\text{m}^{-2}$ , and  $629.7 \text{ Bq}\cdot\text{m}^{-2}$ , respectively) were significantly smaller than the inferred CRI value interval, and the profile distribution pattern of the  $^{137}\text{Cs}$  specific activity was complex and differed from the common distribution pattern of a “negative index”, or “single peak + negative exponential curve”, or “uniform distribution of each layer”. Therefore, by combining total the CPI and  $^{137}\text{Cs}$  profile distribution, it is assumed that the above three sample plots may had experienced more complex soil erosion and soil accumulation processes due to anthropogenic activities, but the overall process is dominated by soil erosion.

Overall, the distribution patterns of the  $^{137}\text{Cs}$  profiles at the sampling plots were closely related to their land-use characteristics. The  $^{137}\text{Cs}$  profile distribution at the sample plots located in grassland and sandy grassland (ZXB-1, ZXB-2, ZXB-4, ZXB-5, ZXB-6, ZXB-7, TPS-1, and TPS-3) usually showed a “single peak + negative exponential curve” profile distribution pattern. The peak  $^{137}\text{Cs}$  activity was generally found in the surface or subsurface layer (0–6 cm) of the soil, and the  $^{137}\text{Cs}$  specific activity decreased gradually with increasing soil depth. In the sample plots located on cultivated land (TPS-2 and TPS-4),

$^{137}\text{Cs}$  showed a uniform distribution pattern in the plow layer (0–20 cm), and the  $^{137}\text{Cs}$  specific activity did not change significantly with soil depth. At the sample plots located in fallow land (TPS-5, TPS-6 and TPS-7), the  $^{137}\text{Cs}$  specific activity was often influenced by a combination of anthropogenic and natural factors, and its profile distribution pattern was more complex, without any uniform and obvious pattern.

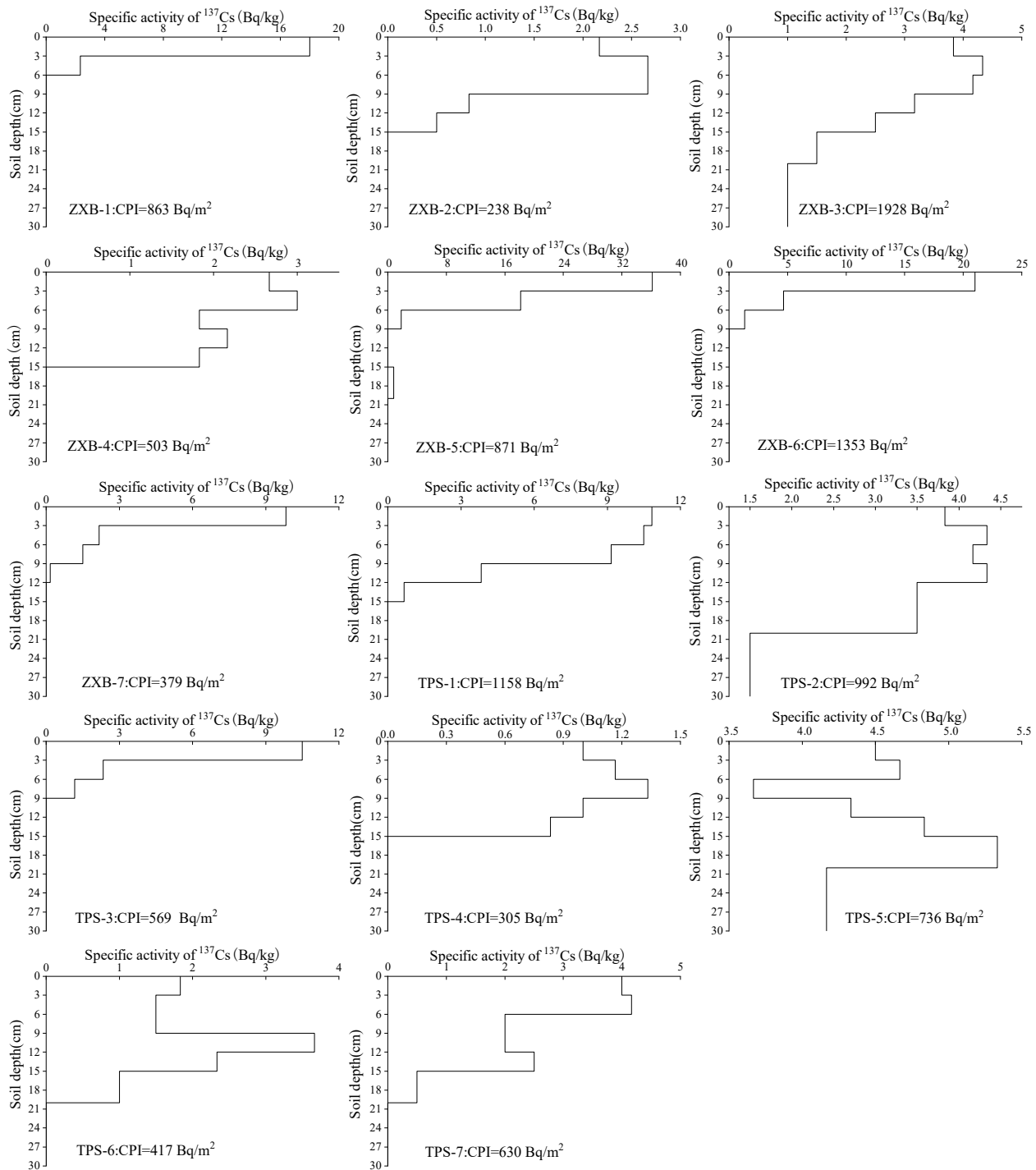


**Figure 2.** The  $^{137}\text{Cs}$  distribution patterns and CPI in the sample plots.

### 3.2. $^{210}\text{Pb}_{\text{ex}}$ Distribution Characteristics and Reference Inventory

We investigated the profile distribution patterns of  $^{210}\text{Pb}_{\text{ex}}$  in the sample plots (Figure 3). In general, the maximum depth of  $^{210}\text{Pb}_{\text{ex}}$  in soil was generally higher than that of  $^{137}\text{Cs}$  in soil.

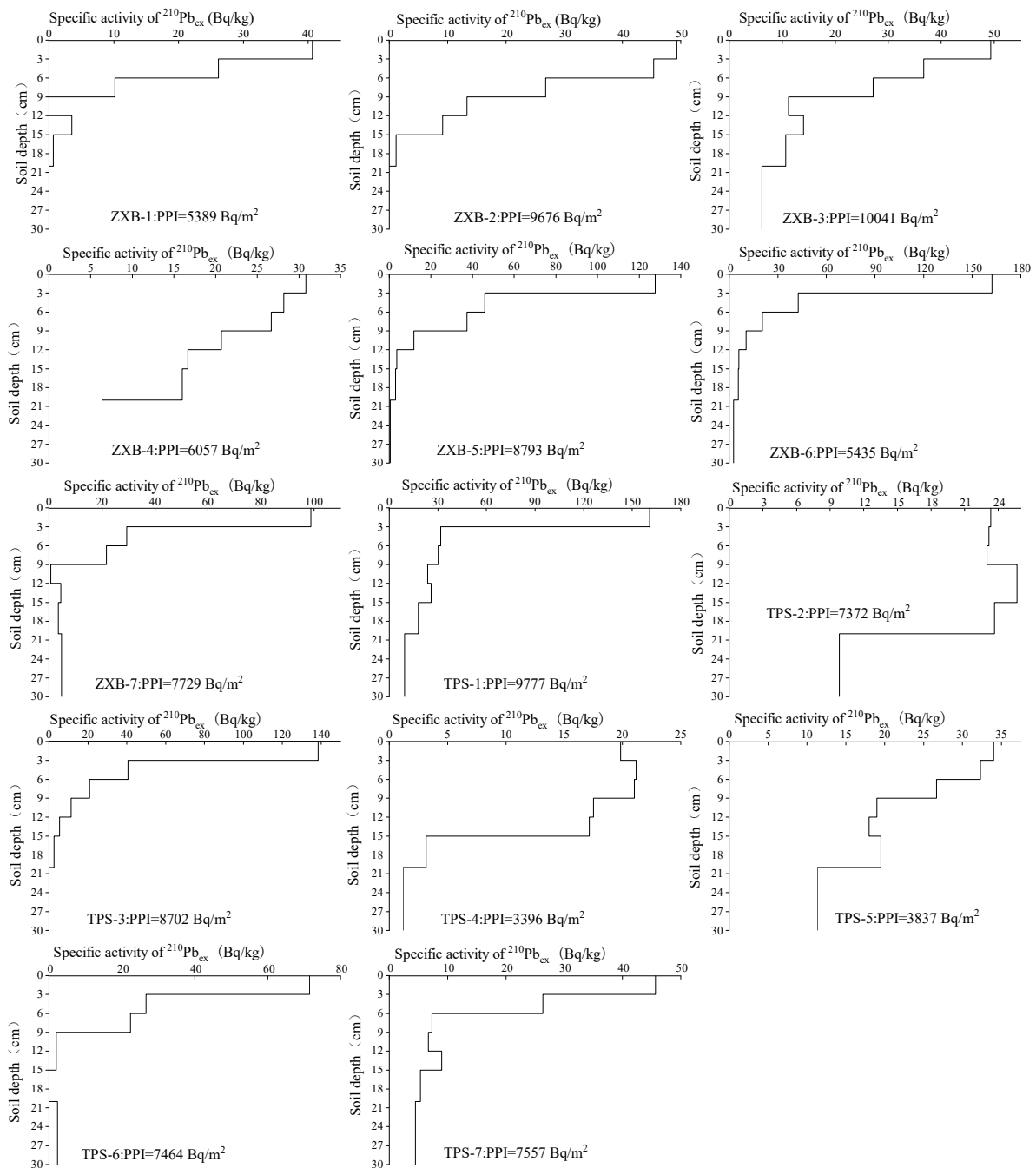


**Figure 3.** The  $^{210}\text{Pb}_{\text{ex}}$  distribution patterns and PPI in the sample plots.

The results showed that  $^{210}\text{Pb}_{\text{ex}}$  was still present in the soil layers below 30 cm in grassland (ZXB-3), semi-shifting sandy land (ZXB-4), as well as in cultivated land (TPS-2, TPS-4) and fallow land (TPS-5, TPS-7).

In the grassland (ZXB-1, ZXB-3, TPS-1, TPS-3), fixed, or semi-fixed sandy land (ZXB-2, ZXB-4, ZXB-5, ZXB-6, ZXB-7),  $^{210}\text{Pb}_{\text{ex}}$  basically showed a complete “negative exponential curve” distribution. The peak activity of  $^{210}\text{Pb}_{\text{ex}}$  was usually found at the 0–3 cm depth of the profile, and the specific activity of  $^{210}\text{Pb}_{\text{ex}}$  decreased gradually with increasing depth

of the profile. Unlike the “single peak + negative exponential curve” pattern of  $^{137}\text{Cs}$  in grassland, the profile distribution of  $^{210}\text{Pb}_{\text{ex}}$  only had a “negative exponential curve” distribution pattern.

In the two sample plots (TPS-2 and TPS-4) located on cultivated land,  $^{210}\text{Pb}_{\text{ex}}$  showed approximately equal activity from the surface layer to 20 cm depth, while, with increasing soil depth,  $^{210}\text{Pb}_{\text{ex}}$  showed less activity, even close to 0 in soils deeper than 20 cm. This reflects the “mixing” process caused by plowing.

In the three sample plots (TPS-5, TPS-6, and TPS-7) located in fallow land, the distribution of  $^{210}\text{Pb}_{\text{ex}}$  was still homogenized by plowing in the deeper soil layer (9–30 cm), but in the upper soil layer (0–9 cm), the spatial distribution of  $^{210}\text{Pb}_{\text{ex}}$  clearly showed a “negative exponential” distribution pattern.

In the previous section, sample plot ZXB-3 was identified as a background plot based on  $^{137}\text{Cs}$  activity,  $^{137}\text{Cs}$  profile distribution, and land-cover information. Therefore, the PPI of sample plot ZXB-3 ( $10,041.2 \text{ Bq}\cdot\text{m}^{-2}$ ) is naturally regarded as the PRI.

### 3.3. Soil Erosion Modulus

Based on the qualitative analysis in Table 2 and Figure 2, the CPI of all sample points (except reference point ZXB-3) was less than the CRI value, indicating different intensities of soil erosion in the above sample plots. According to the  $^{137}\text{Cs}$  soil erosion modulus measurement model (Equations (3)–(5)), the average annual erosion thickness at each plot ranged from 0.1 to 0.7  $\text{mm}\cdot\text{a}^{-1}$  on a 50-year scale, and the erosion modulus ranged from 139.9 to 1029.5  $\text{t}\cdot\text{km}^{-2}\cdot\text{a}^{-1}$  (Table 2).

**Table 2.**  $^{137}\text{Cs}$  activity and soil erosion modulus estimated by the  $^{137}\text{Cs}$  tracing technique.

Plot	Soil	Topography and Land Use	Vegetation Coverage (%)	$^{137}\text{Cs}$ Activity ( $\text{Bq}\cdot\text{m}^{-2}$ )	Soil Bulk Density ( $\text{t}\cdot\text{m}^{-3}$ )	Erosion Thickness ( $\text{mm}\cdot\text{a}^{-1}$ )	Erosion Modulus ( $\text{t}\cdot\text{km}^{-2}\cdot\text{a}^{-1}$ )	Erosion Intensity
ZXB-1	Chestnut soil	Grassland	30~40	$863.1 \pm 139$	1.39	0.3	371.8	Light erosion
ZXB-2	Aeolian sandy soil	Semi-shifting sandy land Grassland	30~40	$238.3 \pm 95$	1.42	0.7	1029.5	Light erosion
ZXB-4	Aeolian sandy soil	Semi-shifting sandy land Grassland	70~80	$502.7 \pm 50$	1.50	0.5	688.4	Light erosion
ZXB-5	Chestnut soil	Fixed sandy land Grassland	70~80	$871 \pm 103$	1.24	0.3	326.5	Light erosion
ZXB-6	Chestnut soil	Fixed sandy land Grassland	70~80	$1353.4 \pm 130$	1.30	0.1	139.9	Slight erosion
ZXB-7	Chestnut soil	Semi-shifting sandy land Grassland	50~60	$378.9 \pm 101$	1.51	0.6	843.1	Light erosion
TPS-1	Chestnut soil	Grassland	50~60	$1158.4 \pm 139$	1.39	0.2	224.8	Light erosion
TPS-2	Chestnut soil	Cultivated land	30~40	$991.9 \pm 134$	1.60	0.2	348.3	Light erosion
TPS-3	Chestnut soil	Grassland	70~80	$568.5 \pm 109$	1.31	0.4	541.9	Light erosion
TPS-4	Chestnut soil	Cultivated land	30~40	$304.5 \pm 46$	1.40	0.6	890.2	Light erosion
TPS-5	Meadow soil	Fallow land	30~40	$735.6 \pm 119$	1.19	0.3	384.2	Light erosion
TPS-6	Chestnut soil	Fallow land	30~40	$417.1 \pm 87$	1.31	0.5	688.1	Light erosion
TPS-7	Chestnut soil	Fallow land	30~40	$629.7 \pm 75$	1.51	0.4	569.6	Light erosion

Note: Erosion intensity was determined by the Standards for Classification and Gradation of Soil Erosion (SL190-96).

Specifically, sample plot ZXB-6, located in fixed sandy land with high vegetation cover, had the highest  $^{137}\text{Cs}$  area activity ( $1353.4 \text{ Bq}\cdot\text{m}^{-2}$ ) and the lowest annual average erosion modulus ( $139.9 \text{ t}\cdot\text{km}^{-2}\cdot\text{a}^{-1}$ ). In contrast, sample plot ZXB-2, located in a semi-shifting sandy land with a wind-sand soil type, had the lowest  $^{137}\text{Cs}$  area activity ( $238.3 \text{ Bq}\cdot\text{m}^{-2}$ ) and the highest annual average erosion modulus ( $1029.5 \text{ t}\cdot\text{km}^{-2}\cdot\text{a}^{-1}$ ). The soil erosion modulus in this area is closely related to land cover, land-use history, and vegetation coverage.

It can also be seen from Table 2 that the sample plots of the semi-shifting sandy land and fixed sandy land (ZXB-2, ZXB-4, ZXB-5, ZXB-6, ZXB-7) usually had the highest

soil erosion modulus, with an average soil erosion modulus of  $605.5 \text{ t}\cdot\text{km}^{-2}\cdot\text{a}^{-1}$ . The second was the samples (TPS-2, TPS-4, TPS-5, TPS-6, TPS-7) from the cultivated and fallow land, which are more influenced by anthropogenic disturbance, showing an average soil erosion modulus of  $576.1 \text{ t}\cdot\text{km}^{-2}\cdot\text{a}^{-1}$ . Finally, the lowest soil erosion modulus occurred in the medium- and high-cover grassland areas (ZXB-1, TPS-1, TPS-3), where the surface vegetation can resist wind and sand erosion to a certain extent, with an average value of  $379.5 \text{ t}\cdot\text{km}^{-2}\cdot\text{a}^{-1}$ .

Based on the same principle, the PPI of all sample points (except the background point ZXB-3) was smaller than the PRI (Table 3), indicating different intensities of soil erosion in the above sample points at the century scale. According to the  $^{210}\text{Pb}_{\text{ex}}$  soil erosion modulus measurement model (Equations (6)–(8)), the average annual erosion thickness at each plot ranged from  $0.02$  to  $1.9 \text{ mm}\cdot\text{a}^{-1}$  and the erosion modulus ranged from  $34.9$  to  $2637.9 \text{ t}\cdot\text{km}^{-2}\cdot\text{a}^{-1}$  at the century scale (Table 3).

**Table 3.**  $^{210}\text{Pb}_{\text{ex}}$  activity and soil erosion modulus estimated by the  $^{210}\text{Pb}_{\text{ex}}$  tracing technique.

Plot	Soil	Topography and Land Use	Vegetation Coverage (%)	$^{210}\text{Pb}_{\text{ex}}$ Activity ( $\text{Bq}\cdot\text{m}^{-2}$ )	Soil Bulk Density ( $\text{t}\cdot\text{m}^{-3}$ )	Erosion Thickness ( $\text{mm}\cdot\text{a}^{-1}$ )	Erosion Modulus ( $\text{t}\cdot\text{km}^{-2}\cdot\text{a}^{-1}$ )	Erosion Intensity
ZXB-1	Chestnut soil	Grassland	30~40	$5388.6 \pm 2116$	1.39	0.8	1139.1	Light erosion
ZXB-2	Aeolian sandy soil	Semi-shifting sandy land Grassland	30~40	$9675.9 \pm 2339$	1.42	0.03	50.2	Slight erosion
ZXB-4	Aeolian sandy soil	Semi-shifting sandy land Grassland	70~80	$6057.1 \pm 652$	1.50	0.6	931.9	Light erosion
ZXB-5	Chestnut soil	Fixed sandy land Grassland	70~80	$8793.2 \pm 3432$	1.24	0.1	164.6	Slight erosion
ZXB-6	Chestnut soil	Fixed sandy land Grassland	70~80	$5435.3 \pm 5564$	1.30	0.8	1045.9	Light erosion
ZXB-7	Chestnut soil	Semi-shifting sandy land Grassland	50~60	$7728.5 \pm 467$	1.51	0.3	423.7	Light erosion
TPS-1	Chestnut soil	Grassland	50~60	$9776.6 \pm 2141$	1.39	0.02	34.9	Slight erosion
TPS-2	Chestnut soil	Cultivated land	30~40	$7372.1 \pm 1459$	1.60	0.3	544.6	Light erosion
TPS-3	Chestnut soil	Grassland	70~80	$8702.4 \pm 843$	1.31	0.1	188.1	Slight erosion
TPS-4	Chestnut soil	Cultivated land	30~40	$3396.3 \pm 1951$	1.40	1.9	2637.9	Moderate erosion
TPS-5	Meadow soil	Fallow land	30~40	$3837.0 \pm 1377$	1.19	1.5	1840.2	Light erosion
TPS-6	Chestnut soil	Fallow land	30~40	$7464.1 \pm 1231$	1.31	0.3	425.2	Light erosion
TPS-7	Chestnut soil	Fallow land	30~40	$7556.5 \pm 1070$	1.51	0.3	464.5	Light erosion

Note: Erosion intensity was determined by the Standards for Classification and Gradation of Soil Erosion (SL190-96).

Among them, the sample plot (TPS-4) on the cultivated land with chestnut soil and lower vegetation coverage had the lowest  $^{210}\text{Pb}_{\text{ex}}$  area activity ( $3396.3 \text{ Bq}\cdot\text{m}^{-2}$ ) and the highest average annual erosion modulus ( $2637.9 \text{ t}\cdot\text{km}^{-2}\cdot\text{a}^{-1}$ ). In contrast, the sample plot (TPS-1) with medium vegetation coverage had the highest  $^{210}\text{Pb}_{\text{ex}}$  area activity ( $9776.6 \text{ Bq}\cdot\text{m}^{-2}$ ) and the lowest average annual erosion modulus ( $34.9 \text{ t}\cdot\text{km}^{-2}\cdot\text{a}^{-1}$ ).

In contrast to the soil erosion modulus regulations at the 50-year scale obtained from the  $^{137}\text{Cs}$  measurements, the sample plots located on the cultivated and fallow lands (TPS-2, TPS-4, TPS-5, TPS-6, TPS-7) had the largest average soil erosion modulus ( $1182.5 \text{ Bq}\cdot\text{m}^{-2}$ ) at the past 100-year scale, indicating that complex human land reclamation activities lead to more intense soil erosion processes. Furthermore, the sample plots located on semi-shifting sandy land and fixed sandy land (ZXB-2, ZXB-4, ZXB-5, ZXB-6, ZXB-7) had an average soil erosion modulus of  $523.3 \text{ Bq}\cdot\text{m}^{-2}$ . Similar to the above findings, the sample plots located in medium and high grassland coverage areas (ZXB-1, TPS-1, TPS-3) had the lowest average soil erosion modulus ( $454 \text{ Bq}\cdot\text{m}^{-2}$ ).

### 3.4. Changes in Soil Erosion and Accumulation Modulus

According to Equation (9), after obtaining the average soil erosion modulus at the 100-year scale (i.e., since the 1920s) based on the  $^{210}\text{Pb}_{\text{ex}}$  soil tracer, and the soil erosion modulus at the 50-year scale (i.e., since the 1970s) based on the  $^{137}\text{Cs}$  soil tracer, the soil erosion modulus from the 1920s–1970s in the 20th century can be further inferred (Figure 4). According to the changes in the soil erosion modulus, all 13 erosion sample plots were divided into three categories.

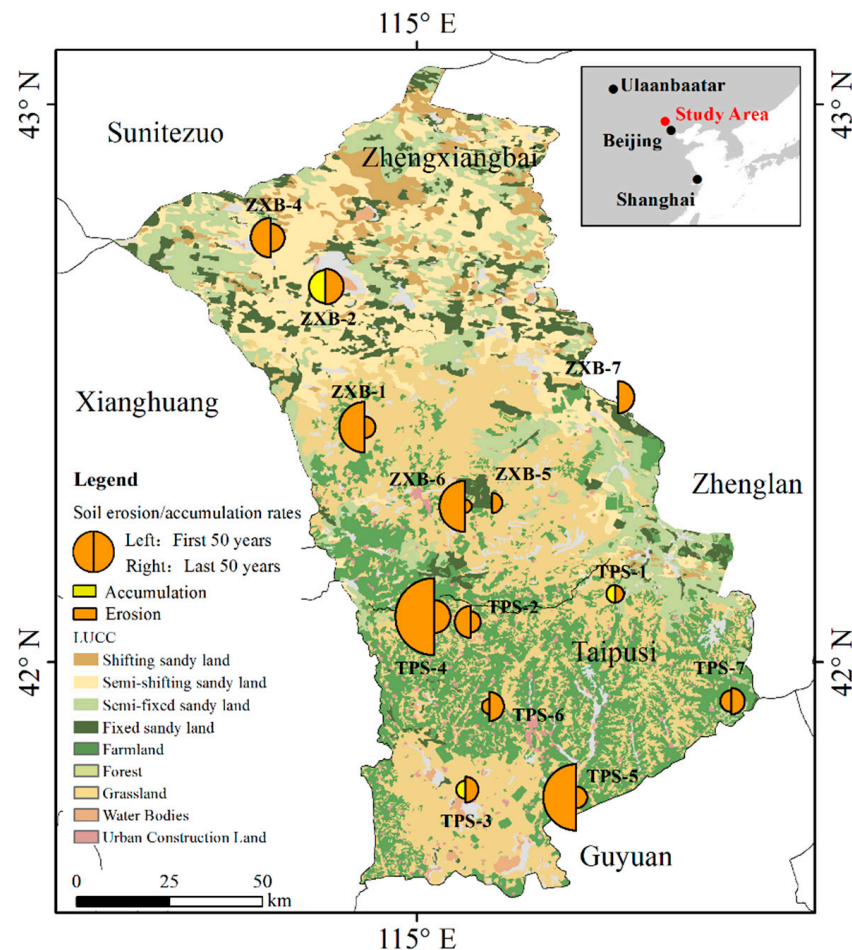


**Figure 4.** Spatial patterns of soil erosion and accumulation modulus changes at the sample plots.

There are six plots (ZXB-1, ZXB-4, ZXB-6, TPS-2, TPS-4, and TPS-5) in the first category. In the past 100 years, there has been a continuous erosion trend, but the erosion intensity has decreased in the past 50 years. The soil erosion modulus since the 1970s has been 40–92% that of the previous period. In terms of spatial distribution, the above sample plots are mainly distributed in the central grassland area and southern cultivated area of the study area.

There are four plots (ZXB-5, ZXB-7, TPS-6 and TPS-7) in the second category. They showed continuous erosion over the past 100 years, but the intensity of erosion has intensified over the past 50 years, mainly in the cultivated land of the southern area and the semi-shifting sandy land of the northern area. In particular, sample plots ZXB-5 and ZXB-7 changed from a state of basically no erosion or no accumulation to a mildly eroded state. However, in general, the erosion amount of these two plots was not high.

There are three plots (ZXB-2, TPS-1, and TPS-3) in the third category, where the soil process is converted from soil accumulation to erosion, and the erosion modulus was higher than that of the accumulation process. In terms of spatial distribution, the above sample plots are mainly distributed in the semi-shifting sandy areas in the northern region,

cultivated land, and grassland of the southern area. This indicates that these sample plots have undergone a more complex soil erosion or accumulation process.

In summary, the southern part of the study area (cultivated land and grassland) was generally dominated by erosion processes. With the 1970s as the boundary, the soil erosion modulus in the former period is smaller than that in the latter period, which indicates that land reclamation and grassland grazing practices in the southern area may have intensified the soil erosion process. In the northern part of the study area (sandy grassland dominated by fixed and semi-fixed sandy land), both soil accumulation and soil erosion were present. The soil erosion or accumulation modulus after 1970 was generally lower than the previous period, indicating that wind and sand activities in the northern area had weakened.

#### 4. Discussion

Accurate determination of regional  $^{137}\text{Cs}$  and  $^{210}\text{Pb}_{\text{ex}}$  background values and a reference inventory are the scientific basis for the quantitative assessment of soil erosion by applying  $^{137}\text{Cs}$  and  $^{210}\text{Pb}_{\text{ex}}$  composite tracer techniques. However, there are uncertainties in this process, which involves the following aspects. The study area, which is in the farming–pastoral ecotone in northern China, experienced complicated land-cover changes and human activities, such as cultivation–abandonment and grassland grazing–abandonment alternate states, leading to uncertainties in the backgrounds of the sample plots. Frequent dune consolidation activities lead to the formation of either blown-out or wind-sand soil accumulation. In the wind-sand area, the distribution of tracer isotopes vary greatly in plane and profile. In some sites, the isotope cannot be detected at all, while in other sites the depth of the isotope distribution exceeds 30 cm. The slope may also affect the isotopic content of the soil surface; for example, the  $^{137}\text{Cs}$  content in the upper or steep slope will be lower than that in the middle and lower slopes [43]. The geomorphology of the study area in this paper mainly includes a high plain grassland or sand dune geomorphology, and the gradient fluctuation is relatively small. In addition,  $^{137}\text{Cs}$  in soils become increasingly difficult to detect over time due to the single source and a short half-life, and  $^{210}\text{Pb}_{\text{ex}}$  comes through multiple decay processes of  $^{226}\text{Ra}$ ,  $^{222}\text{Rn}$ , and  $^{238}\text{U}$ , resulting in the complex measurement process of  $^{210}\text{Pb}_{\text{ex}}$  [44]. It should be noted that it is difficult to separate the two isotope particles after they are combined with fine particles. The activity of  $^{137}\text{Cs}$  is mainly related to the local rainfall, and the activity of  $^{210}\text{Pb}_{\text{ex}}$  is mainly affected by the local geological structure and rock stratum type. Both particles are mainly distributed in the soil layer above 30 cm in the soil profile, and their content in the soil is very low. Therefore, due to the above characteristics, isotope particles such as  $^{137}\text{Cs}$  and  $^{210}\text{Pb}_{\text{ex}}$  will not affect the ecological environment of the soil, nor will they threaten the safety of humans and animals.

In this study, various characteristics, such as the land cover, theoretical simulation values, and profile distribution pattern of  $^{137}\text{Cs}$ , were considered to determine ZXB-3 as the background plot and the corresponding CRI value ( $1927.9 \text{ Bq}\cdot\text{m}^{-2}$ ). Compared with the previous results in adjacent areas (CRI values for different years were uniformly modified to 2018:  $1740.1 \text{ Bq}\cdot\text{m}^{-2}$  in Miyun of Beijing,  $1690.3 \text{ Bq}\cdot\text{m}^{-2}$  in Dehui of Jilin,  $1712.8 \text{ Bq}\cdot\text{m}^{-2}$  in Jiutai of Jilin,  $1947 \text{ Bq}\cdot\text{m}^{-2}$  in Keshan of Heilongjiang,  $1938.7 \text{ Bq}\cdot\text{m}^{-2}$  in Hunsandake of Inner Mongolia,  $1994.8 \text{ Bq}\cdot\text{m}^{-2}$  in Xingan of Inner Mongolia,  $1930.4 \text{ Bq}\cdot\text{m}^{-2}$  in Xilingol of Inner Mongolia, and  $1980.9 \text{ Bq}\cdot\text{m}^{-2}$  in Tongliao and Chifeng of Inner Mongolia) [24,25,43,45,46], the CRI value obtained in this study is within the ranges of geographically adjacent CRI values and has considerable credibility. In this paper, the  $^{137}\text{Cs}$  background plot (ZXB-3) was also used as the  $^{210}\text{Pb}_{\text{ex}}$  background plot to obtain the PRI value ( $10,041.2 \text{ Bq}\cdot\text{m}^{-2}$ ), which is higher compared to the results from adjacent areas ( $6600 \text{ Bq}\cdot\text{m}^{-2}$  in Keshan of Heilongjiang,  $5730 \text{ Bq}\cdot\text{m}^{-2}$  in the Loess Plateau, and  $8112 \text{ Bq}\cdot\text{m}^{-2}$  in Hunsandake, Inner Mongolia) [25,41]. In fact, considering the fact that traces were detected in the soil layer below 30 cm in the ZXB-3 site (Figure 3), the PRI in this study may be higher. The reason may be that the continuous sedimentation of  $^{210}\text{Pb}_{\text{ex}}$  resulted in more accumulation of  $^{210}\text{Pb}_{\text{ex}}$ .

The soil erosion modulus ranged from  $139.9 \text{ t}\cdot\text{km}^{-2}\cdot\text{a}^{-1}$  to  $1029.5 \text{ t}\cdot\text{km}^{-2}\cdot\text{a}^{-1}$  for grasslands and sandy grasslands in the study area based on  $^{137}\text{Cs}$  isotope tracing. It is higher than the previous studies conducted in Tariat–Bayannur–Xilingol of the Mongolian Plateau ( $64.58 \text{ t}\cdot\text{km}^{-2}\cdot\text{a}^{-1}$  to  $419.6 \text{ t}\cdot\text{km}^{-2}\cdot\text{a}^{-1}$ ) [26,47]. This is related to the fact that the study area is located at the southern margin of the Hunsandake sandy area, where there are many fixed and semi-fixed sandy lands. Compared with the results of the abandoned land (Harahalin:  $6723.06 \text{ t}\cdot\text{km}^{-2}\cdot\text{a}^{-1}$ ) in the northern part of the Tariat–Bayannur–Xilingol sample zone [26,47], the soil erosion modulus on the cultivated and fallow land in this study was lower ( $348.2\text{--}890.2 \text{ t}\cdot\text{km}^{-2}\cdot\text{a}^{-1}$ ) due to weaker winds and the presence of conservation tillage and shelterbelts in the study area.

In this study, changes in the soil erosion modulus were estimated for the past 100- and 50-year scales. In the southern part of the study area (cultivated land and grassland), the land reclamation and grassland grazing activities promoted the rate of soil erosion, while in the northern part of the study area (marginal area of Hunsandake sandy land), there is a slowing down trend in the soil erosion modulus due to climate change (weaker wind and more precipitation) [48]. This is consistent with previous findings, showing there is a slowdown in the soil erosion modulus and even a shift from erosion to accumulation processes at most sample plots in the Hunsandake sandy land [25]. These new quantitative findings provide new evidence for understanding the impacts of climate change, physical-geographical changes, and human activities in the farming–pastoral ecotone in northern China.

Considering that the Chinese government has carried out large-scale ecological restoration and treatment projects in the region over the past 20 years (since 2000) (e.g., the Beijing–Tianjin Sand Source Control project, Three-North Shelter Forest program, Returning Grazing Land, and the Natural Forest Protection project), the measurement of the soil erosion characteristics' changes in the two periods before and after 2000 is an important basis for evaluating the effectiveness of ecosystem construction projects. However, current soil erosion measurement techniques based on  $^{137}\text{Cs}$  and  $^{210}\text{Pb}_{\text{ex}}$  cannot support this goal. In fact, after determining the background plots, we can qualitatively and roughly analyze soil erosion and accumulation processes in recent years based on the isotope distribution characteristics in soil profiles. A more reliable method is to develop soil tracing and erosion rate measurement techniques based on  $^7\text{Be}$  because of the characteristics of  $^7\text{Be}$  as a natural radionuclide with a shorter half-life (53.3d) [49].

## 5. Conclusions

Given that it is difficult to scientifically determine a regional background sample plot, accurately estimate a regional reference inventory, and measure the soil erosion modulus at different periods, a multi-isotope ( $^{137}\text{Cs}$  and  $^{210}\text{Pb}_{\text{ex}}$ ) composite tracing technique was applied in this paper to measure the soil erosion modulus. This study has deepened and further developed traditional single soil tracer isotope ( $^{137}\text{Cs}$  or  $^{210}\text{Pb}_{\text{ex}}$ ) research, and the results provide quantitative scientific evidence for understanding climate change, physical and geographical changes, and the impact of human activities in the agropastoral interlaced zone in northern China. The main conclusions are as follows: (1) considering the land-cover/utilization type, total isotope amount, isotope profile distribution, and other characteristic information of the sample points, combined with the theoretical model calculation results and the underestimated range, this paper scientifically and reasonably demarcates the regional background points, and determines that the background values of  $^{137}\text{Cs}$  and  $^{210}\text{Pb}_{\text{ex}}$  in the study area are  $1928 \text{ Bq}\cdot\text{m}^{-2}$  and  $10,041 \text{ Bq}\cdot\text{m}^{-2}$ , respectively; (2) considering that  $^{137}\text{Cs}$  and  $^{210}\text{Pb}_{\text{ex}}$  have a different sedimentation duration and isotope half-life, it was found that the study area is generally in a lightly eroded state at the 100-year scale and 50-year scale by comprehensively using the above two isotope-tracing methods; and (3) the soil erosion modulus in the southern and northern parts of the study area tended to increase and decrease, respectively. From the comparison with relevant results in the literature, the background values, soil erosion rate modulus, and other results obtained

in this study are reliable. The technical route and research methods of using composite isotopes to trace the soil erosion rate are increasingly mature, which has important reference value for similar research in other regions of the world in the future.

**Author Contributions:** Data curation, Y.Z.; Formal analysis, X.G.; Funding acquisition, Y.H.; Supervision, Y.H.; Writing—original draft, X.G.; Writing—review & editing, Y.H. and L.Z. All authors have read and agreed to the published version of the manuscript.

**Funding:** This research was funded by National Natural Science Foundation of China (grant number: 41977421) and Strategic Priority Research Program of the Chinese Academy of Sciences (grant number: XDA20010202). The APC was funded by (41977421).

**Institutional Review Board Statement:** Not applicable.

**Informed Consent Statement:** Not applicable.

**Data Availability Statement:** Not applicable.

**Conflicts of Interest:** The authors declare no conflict of interest.

## References

1. Vanmaercke, M.; Poesen, J.; Maetens, W.; de Vente, J.; Verstraeten, G. Sediment yield as a desertification risk indicator. *Sci. Total Environ.* **2011**, *409*, 1715–1725. [[CrossRef](#)] [[PubMed](#)]
2. Ye, D.; Chou, J.; Liu, J.; Zhang, Z.; Wang, Y.; Zhou, Z.; Ju, H.; Huang, Q. Causes of sand-stormy weather in Northern China and Control Measures. *Acta Geogr. Sin.* **2000**, *5*, 513–521.
3. Batunacun, Nendel, C.; Hu, Y.; Lakes, T. Land-use change and land degradation on the Mongolian Plateau from 1975 to 2015—A case study from Xilingol, China. *Land Degrad. Dev.* **2018**, *29*, 1595–1606. [[CrossRef](#)]
4. Lu, F.; Hu, H.; Sun, W.; Zhu, J.; Liu, G.; Zhou, W.; Zhang, Q.; Shi, P.; Liu, X.; Wu, X.; et al. Effects of national ecological restoration projects on carbon sequestration in China from 2001 to 2010. *Proc. Natl. Acad. Sci. USA* **2018**, *115*, 4039–4044. [[CrossRef](#)]
5. Wang, J.; Su, Z.; Zhou, T.; Wang, L.; Wang, X.; Liu, Y.; Wu, Z. Cs-137 and Pb-210(ex) tracing of soil erosions on cultivated and reforested slope lands in Three North-Shelter Forest Region. *Trans. Chin. Soc. Agric. Eng.* **2020**, *36*, 64–72.
6. Huang, J.; Yao, Z.H.; Zha, S.X.; Xiao, P.Q.; Wang, B. Progress of study on soil and water conservation measure factors in USLE/RUSLE. *Soil Water Conserv. China* **2020**, *3*, 37–39.
7. Zhang, Z.G.; Hua, L.; Feng, Y.; Zhao, H.; Fu, H.; Zhu, F.Y.; Liu, J.Z. Research progress on soil erosion by using (137) Cs Nuclear tracer. *J. Cap. Norm. Univ.* **2003**, *20*, 82–87.
8. Liu, N.; Wang, K.L.; Zhang, W.; Zhang, X.N. Progress on the study of soil erosion, evaluation, and validation. *Chin. Agric. Sci. Bull.* **2011**, *27*, 1–6.
9. Zambon, N.; Johannsen, L.L.; Strauss, P.; Dostal, T.; Zimr, D.; Cochrane, T.A.; Klik, A. Splash erosion affected by initial soil moisture and surface conditions under simulated rainfall. *Catena* **2021**, *196*, 104827. [[CrossRef](#)]
10. Menzel, R.G. Transport of Strontium-90 in Runoff. *Science* **1960**, *131*, 499–500. [[CrossRef](#)]
11. Li, Y.; Wang, Z.; Zhao, J.; Lin, Y.; Tang, G.; Tao, Z.; Gao, Q.; Chen, A. Characterizing soil losses in China using data of Cs-137 inventories and erosion plots. *Catena* **2021**, *203*, 105296. [[CrossRef](#)]
12. Meliho, M.; Noura, A.; Benmansour, M.; Boulmane, M.; Khattabi, A.; Mhammdi, N.; Benkdad, A. Assessment of soil erosion rates in a Mediterranean cultivated and uncultivated soils using fallout 137Cs. *J. Environ. Radioact.* **2019**, *208*, 106021. [[CrossRef](#)] [[PubMed](#)]
13. Royall, D. Use of mineral magnetic measurements to investigate soil erosion and sediment delivery in a small agricultural catchment in limestone terrain. *Catena* **2001**, *46*, 15–34. [[CrossRef](#)]
14. Schoorl, J.M.; Boix Fayos, C.; de Meijer, R.J.; van der Graaf, E.R.; Veldkamp, A. The Cs-137 technique applied to steep Mediterranean slopes (Part I): The effects of lithology, slope morphology and land use. *Catena* **2004**, *57*, 15–34. [[CrossRef](#)]
15. Walling, D.E.; Quine, T.A. Use of 137cs Measurements to Investigate Soil-Erosion on Arable Fields in the Uk—Potential Applications and Limitations. *J. Soil Sci.* **1991**, *42*, 147–165. [[CrossRef](#)]
16. Zhang, X.; Higgitt, D.L.; Walling, D.E. A preliminary assessment of the potential to use Cs-137 to estimate the rates of soil erosion in the Loess Plateau of China. *Geochimica* **1991**, *3*, 212–218.
17. Li, R.; Yang, H.; Zhao, X.; Tang, X. Application of Cs-137 technique to study of soil erosion on Loess Plateau region. *Soils* **2004**, *1*, 96–98.
18. Wang, X.; Xue, B.; Yao, S.; Yang, H.; Gu, Z.; Yang, B.; Zhang, M.; Zhu, Y. Cs-137 estimates of soil erosion rates in a small catchment on a channelized river floodplain in the lower reaches of Yangtze River, China. *J. Environ. Radioact.* **2019**, *208–209*, 106008. [[CrossRef](#)]
19. Wen, A.; Zhang, X.; Wang, Y.; Feng, M.; Zhang, Y.; Xu, J.; Bai, L.; He, T.; Wang, J. Study on soil erosion rates using Cs-137 technique in Upper Yangtze River. *J. Soil Water Conserv.* **2002**, *6*, 1–3.

20. He, Y.; Zhang, F.; Yang, M. Effects of soil erosion on organic carbon fractions in black soils in sloping farmland of Northeast China by using Cs-137 tracer measurements. *Trans. Chin. Soc. Agric. Eng.* **2021**, *37*, 60–68.
21. Song, R.; Hu, K.; Guo, J.; Wu, C. Applications of Cs-137 to quantitative evaluation of soil erosion in Northeast Songnen Plain. *Chin. J. Grassl.* **2005**, *20*, 11–14.
22. Yan, P.; Dong, G.R.; Zhang, X.B.; Zhang, Y.Y. Preliminary results of the study on wind erosion in the Qinghai-Tibetan Plateau using Cs-137 technique. *Chin. Sci. Bull.* **2000**, *45*, 1019–1025. [[CrossRef](#)]
23. Tang, X.; Yang, H.; Cao, H.; Zhao, Q.; Li, R. Preliminary estimate of soil erosion rate in Haplic Red Soil in Southern China using Cs-137 technique. *J. Soil Water Conserv.* **2001**, *11*, 4–7.
24. Hu, Y.; Liu, J.; Zhen, L. Determination of Cs-137 reference inventories in a large-scale region: A case study in the central-eastern Inner Mongolia Plateau. *J. Geogr. Sci.* **2014**, *24*, 1047–1059. [[CrossRef](#)]
25. Hu, Y.; Zhang, Y. Using <sup>137</sup>Cs and <sup>210</sup>Pb to investigate the soil erosion and accumulation moduli on the southern margin of the Hunshandake Sandy Land in Inner Mongolia. *J. Geogr. Sci.* **2019**, *29*, 1655–1669. [[CrossRef](#)]
26. Liu, J.; Qi, Y.; Shi, H.; Zhuang, D.; Hu, Y. Estimation of wind erosion rates by using Cs-137 tracing technique: A case study in Tariat-Xilin Gol transect, Mongolian Plateau. *Chin. Sci. Bull.* **2008**, *53*, 751–758. [[CrossRef](#)]
27. Benmansour, M.; Mabit, L.; Nouria, A.; Moussadek, R.; Bouksirate, H.; Duchemin, M.; Benkdad, A. Assessment of soil erosion and deposition rates in a Moroccan agricultural field using fallout Cs-137 and Pb-210(ex). *J. Environ. Radioact.* **2013**, *115*, 97–106. [[CrossRef](#)]
28. Gharbi, F.; AlSheddi, T.H.; Ben Ammar, R.; El-Naggar, M.A. Combination of <sup>137</sup>Cs and <sup>210</sup>Pb Radioactive Atmospheric Fallouts to Estimate Soil Erosion for the Same Time Scale. *Int. J. Environ. Res. Public Health* **2020**, *17*, 8292. [[CrossRef](#)]
29. Kalkan, K.S.; Forkapic, S.; Markovic, S.B.; Bikit, K.; Gavrilov, M.B.; Tosic, R.; Mrda, D.; Lakatos, R. The application of Cs-137 and Pb-210(ex) methods in soil erosion research of Titel loess plateau, Vojvodina, Northern Serbia. *Open Geosci.* **2020**, *12*, 11–24. [[CrossRef](#)]
30. Mabit, L.; Benmansour, M.; Walling, D.E. Comparative advantages and limitations of the fallout radionuclides Cs-137, Pb-210(ex) and Be-7 for assessing soil erosion and sedimentation. *J. Environ. Radioact.* **2008**, *99*, 1799–1807. [[CrossRef](#)]
31. Porto, P.; Walling, D.E.; Callegari, G. Using repeated Cs-137 and Pb-210(ex) measurements to establish sediment budgets for different time windows and explore the effect of connectivity on soil erosion rates in a small experimental catchment in Southern Italy. *Land Degrad. Dev.* **2018**, *29*, 1819–1832. [[CrossRef](#)]
32. Su, Z.A.; Zhou, T.; Zhang, X.B.; Wang, X.Y.; Wang, J.J.; Zhou, M.H.; Zhang, J.H.; He, Z.Y.; Zhang, R.C. A Preliminary Study of the Impacts of Shelter Forest on Soil Erosion in Cultivated Land: Evidence from integrated Cs-137 and Pb-210(ex) Measurements. *Soil Tillage Res.* **2021**, *206*, 104843. [[CrossRef](#)]
33. Walling, D.E.; He, Q. Using fallout lead-210 measurements to estimate soil erosion on cultivated land. *Soil Sci. Soc. Am. J.* **1999**, *63*, 1404–1412. [[CrossRef](#)]
34. Hu, Y.F.; Liu, J.Y.; Zhuang, D.F.; Cao, H.X.; Yan, H.M.; Yang, F.T. Distribution characteristics of (CS)-C-137 in wind-eroded soil profile and its use in estimating wind erosion modulus. *Chin. Sci. Bull.* **2005**, *50*, 1155–1159. [[CrossRef](#)]
35. Walling, D.E.; He, Q. Improved models for estimating soil erosion rates from cesium-137 measurements. *J. Environ. Qual.* **1999**, *28*, 611–622. [[CrossRef](#)]
36. Qi, Y.; Zhang, X.; He, X.; Wen, A.; Fu, J. (<sup>137</sup>Cs) reference inventories distribution pattern in China. *Nucl. Tech.* **2006**, *29*, 42–50.
37. Quine, T.A.; Navas, A.; Walling, D.E.; Machin, J. Soil-erosion and redistribution on cultivated and uncultivated land near las-bardenas in the central ebro river basin, spain. *Land Degrad. Rehabil.* **1994**, *5*, 41–55. [[CrossRef](#)]
38. Chen, R.; Zhang, M.; Yang, H. Dynamic Equilibrium Model of Pb-210(ex) Background Value in Soil. *Res. Soil Water Conserv.* **2013**, *20*, 73–76.
39. Li, J.; Li, Y.; Wang, Y.; Wu, J. Study of Soil Erosion on the East-West Transects in the Three-Rivers Headwaters Region Using Cs-137 and Pb-210(ex) Tracing. *Res. Environ. Sci.* **2009**, *22*, 1452–1459.
40. Yang, Y.H.; Yan, B.X.; Zhu, H. Estimating Soil Erosion in Northeast China Using Cs-137 and Pb-210(ex). *Pedosphere* **2011**, *21*, 706–711. [[CrossRef](#)]
41. Zhang, X.B.; Walling, D.E.; Feng, M.Y.; Wen, A.B. Pb-210(ex) depth distribution in soil and calibration models for assessment of soil erosion rates from Pb-210(ex) measurements. *Chin. Sci. Bull.* **2003**, *48*, 813–818.
42. Sun, W.; Yang, H.; Zhao, Q.; Zhang, M.; Xu, L. Response of Pb-210(ex) inventory to changes in soil erosion rates on uncultivated land. *Chin. Sci. Bull.* **2013**, *58*, 1725–1730. [[CrossRef](#)]
43. Hua, L.; Zhang, Z.; Li, J.; Feng, Y.; Zhao, H.; Yin, X.; Zhu, F. Soil erosion and organic matter loss by using fallout Cs-137 as tracer in MiYun reservoir valley. *J. Nucl. Agric. Sci.* **2005**, *19*, 208–213.
44. Zapata, F. The use of environmental radionuclides as tracers in soil erosion and sedimentation investigations: Recent advances and future developments. *Soil Tillage Res.* **2003**, *69*, 3–13. [[CrossRef](#)]
45. Fang, H.; Yang, X.; Zhang, X.; Liang, A. Study on soil erosion and deposition of black soils on a sloping cultivated land using <sup>137</sup>Cs tracer method. *Acta Ecol. Sin.* **2005**, *25*, 1376–1382.
46. Yan, B.; Tang, J. Study on Cs-137 reference inventory of black soil in Northeast China. *J. Soil Water Conserv.* **2004**, *70*, 33–36.
47. Qi, Y.; Liu, J.; Shi, H.; Hu, Y.; Zhuang, D. Using Cs-137 tracing technique to estimate wind erosion rates in the typical steppe region, northern Mongolian Plateau. *Chin. Sci. Bull.* **2008**, *53*, 1423–1430.

- 
48. Li, X. Analysis of factors to desertification and its significance. *Res. Soil Water Conserv.* **2003**, *3*, 140–141.
  49. Shi, Z.; Wen, A.; Yan, D.; Long, Y.; Zhou, P. Discussion on the use of Be-7 to estimate soil erosion rates. *Adv. Earth Sci.* **2016**, *31*, 885–893.